Journal of Electronic Imaging

JElectronicImaging.org

Texture descriptors based on adaptive neighborhoods for classification of pigmented skin lesions

Víctor González-Castro
Johan Debayle
Yanal Wazaefi
Mehdi Rahim
Caroline Gaudy-Marqueste
Jean-Jacques Grob
Bernard Fertil

SPIE. IS&T imaging.org

Texture descriptors based on adaptive neighborhoods for classification of pigmented skin lesions

Víctor González-Castro,[a] Johan Debayle,[b,*] Yanal Wazaefi,[c] Mehdi Rahim,[c] Caroline Gaudy-Marqueste,[d] Jean-Jacques Grob,[d] and Bernard Fertil[c]
[a]University of Edinburgh, Neuroimaging Sciences, Centre for Clinical Brain Sciences, 49 Little France Crescent, Edinburgh EH6 8SP, United Kingdom
[b]École Nationale Supérieure des Mines de Saint-Étienne, SPIN/LGF UMR CNRS 5307, 158 Cours Fauriel, CS 62362, 42023 Saint-Étienne, France
[c]Laboratoire des Sciences de l'Information et des Systèmes, UMR CNRS 7296, 163 Avenue de Luminy, 13288 Marseille Cedex 9, France
[d]Hôpital de la Timone, Service de Dermatologie, Marseille, 264 rue Saint-Pierre, 13385 Marseille Cedex 5, France

Abstract. Different texture descriptors are proposed for the automatic classification of skin lesions from dermoscopic images. They are based on color texture analysis obtained from (1) color mathematical morphology (MM) and Kohonen self-organizing maps (SOMs) or (2) local binary patterns (LBPs), computed with the use of local adaptive neighborhoods of the image. Neither of these two approaches needs a previous segmentation process. In the first proposed descriptor, the adaptive neighborhoods are used as structuring elements to carry out adaptive MM operations which are further combined by using Kohonen SOM; this has been compared with a nonadaptive version. In the second one, the adaptive neighborhoods enable geometrical feature maps to be defined, from which LBP histograms are computed. This has also been compared with a classical LBP approach. A receiver operating characteristics analysis of the experimental results shows that the adaptive neighborhood-based LBP approach yields the best results. It outperforms the nonadaptive versions of the proposed descriptors and the dermatologists' visual predictions. [DOI: 10.1117/1.JEI.24.6.061104]

Keywords: general adaptive neighborhoods; local binary patterns; mathematical morphology; self-organizing maps; texture description.

Paper 15433SS received May 28, 2015; accepted for publication Aug. 12, 2015; published online Sep. 21, 2015.

1 Introduction

In 2012, there were more than 11,150 new cases of skin cancer in France (3.1% of all detected cancers), 15% of which were mortal. Late diagnosis of skin cancer makes treatments much less efficient (i.e., a melanoma may become very aggressive in just a few months). Therefore, its early detection becomes essential to improve the chances of curing the skin cancer and, thus the patient's chances of survival.

This is not an easy task for a nonexperienced observer, as is shown in Fig. 1. To carry out the detection of melanoma, dermatologists use several state-of-the-art methods, often called "rules," such as the ABCD rule[1]: asymmetry, border irregularity, color irregularity, and differential structure (i.e., the size and number of structural features); or the Menzies scoring, namely the seven-point checklist,[2] which is based on the presence of certain texture patterns. However, although dermatologists could use such analytical pattern recognition rules to predict malignancy, they appear to use more a nonanalytical reasoning, derived through experience of prior examples to identify skin lesions.[3] Some studies suggest that experienced clinicians make a diagnosis intuitively and then they alter their analytical assessment to fit in with their preconceptions about the relationship between these features (e.g., the ABCD) and the diagnosis (e.g., melanoma).[4,5] An automation of individual analyses of nevi would be very helpful not only for dermatologists, as they would make more accurate diagnoses and thus make better decisions about the need of surgery, but also for general practitioners, who could make better decisions about sending patients to the specialist more appropriately. Therefore, it would save economic and time resources of the Social Security system.

Automatic melanoma detection, based on the analysis of dermoscopy images, has been receiving an increasing attention in the literature.[6] Most works reproduce the classic rules used by dermatologists, extracting features linked to them.[7–10] Others go beyond and combine them with other types of characteristics. For example, Rastgoo et al.[11] combine them with bag of words descriptors. However, such types of feature extraction methods needs a previous segmentation of the lesion, which is often a very tricky step for computers, as it may not be clear, even for specialists, where the boundaries of the lesion are. Indeed, even trained dermatologists differ significantly when delineating the same lesion in separate incidents.[12] There are numerous papers devoted to automatic boundary detection of skin lesions.[13–15] Other methods have been investigated in the literature where dermoscopic images do not need any segmentation process as proposed in Ref. 16, where a texture descriptor computed by means of the local binary patterns[17–19] (LBPs) is used. Nevertheless, only intensity information of the color components is taken into consideration.

In this paper, some methods for automatically discriminating between melanoma and benign skin lesions from dermoscopic images without the need of segmentation are proposed. They are based on the general adaptive neighborhood image processing (GANIP) framework.[20,21] The first one is

*Address all correspondence to: Johan Debayle, E-mail: debayle@emse.fr

1017-9909/2015/$25.00 © 2015 SPIE and IS&T

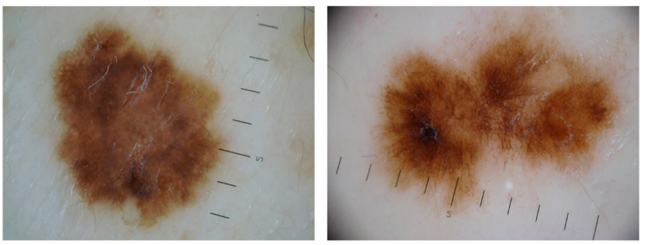

(a) (b)

Fig. 1 Example of an image of a (a) benign lesion and (b) a melanoma.

based on a texture descriptor using color mathematical morphology (MM)[22] and Kohonen self-organizing maps (SOM).[23] The second one is based on a combination of LBPs and local geometrical measurements. Specifically, the lesions are described by means of the LBPs calculated from maps created by means of the geometrical features of the general adaptive neighborhoods (GANs)[20] of pixels.

The rest of the paper is organized as follows: first of all, a detailed explanation of the required methods and tools and how these are used to create the descriptors is given in Secs. 2 and 3, respectively. Afterward, the performance of these descriptors is assessed on a real dataset of skin lesions, as stated in Sec. 4. Finally, conclusions and future perspectives are shown in Sec. 5.

2 Required Methods and Tools

2.1 *General Adaptive Neighborhoods*

The GANIP approach[20,21] provides a general framework for multiscale, local, and adaptive image processing and analysis of gray-level images. It is based on extracting spatial neighborhoods called GANs from the points of the image, whose size and shape are adapted to the local features of the image. Specifically, a GAN is a subset of the spatial support $D \subseteq \mathbb{R}^2$ constituted by connected points whose values in relation to a selected criterion (luminance, contrast, etc.) fit within a homogeneity tolerance. As a result, GANs are adaptive with the spatial structures and are self-defined from the image.

Let f be an image defined in D with range in $\mathbb{R}$, and let h be a "criterion mapping," also defined in D and valued in $\mathbb{R}$, based on local measurements such as luminance, contrast, etc. For each point $x \in D$, the GANs (denoted $V_m^h(x)$) are subsets in D built upon h in relation to a homogeneity tolerance $m \in \mathbb{R}^+$. More precisely, $V_m^h(x)$ fulfills two conditions: (1) its points are close to x in relation to the criterion mapping and (2) the GAN is a path-connected set.

Thus, the GANs are formally defined as

$$V_m^h(x) = C_{\{y \in D : |h(y)-h(x)| \leq m\}}(x), \tag{1}$$

where $C_X(x)$ denotes the path-connected component of $X \subseteq D$ containing $x \in D$. Therefore, it is ensured that $\forall x \in Dx \in V_m^h(x)$.

Figure 2 shows the GAN computed for one pixel of a dermoscopic color image using the luminance criterion of the red color component and the homogeneity tolerance $m = 20$.

However, these GANs do not satisfy the "symmetry property," which is relevant for visual, topological, morphological, and practical reasons,[20] defined as

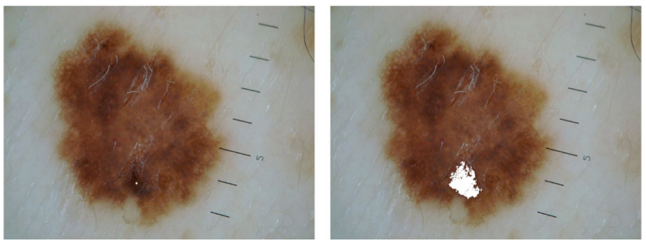

(a) (b)

Fig. 2 The general adaptive neighborhood (GAN) (b) of one pixel (a) of a dermoscopic image computed on the red color component, using the luminance criterion with the homogeneity tolerance value $m = 20$.

$$\forall\, x, y \in D \quad y \in A(x) \Leftrightarrow x \in A(y), \tag{2}$$

where $\{A(x)\}_{x \in D}$ is a collection of subsets $A(x) \subseteq D$. For this reason, GANs defined in Eq. (1) are called weak GANs.

In order to get this property satisfied, a new set of GANs, called strong GANs, is defined as

$$N_m^h(x) = \bigcup_{z \in D} \{V_m^h(z) : x \in V_m^h(z)\}. \tag{3}$$

The reader interested in further theoretical aspects of GANs is referred to Ref. 20.

2.2 *Color Mathematical Morphology*

Morphological operators[24] need the sets of the intensities to be processed to hold a total order relationship. However, in the case of color images, this is not straightforward due to the vectorial nature of their points.

In the literature, several order relationships have been proposed (i.e., marginal, lexicographical, partial, or reduced ordering). In this work, the so-called Ω-ordering—denoted as $\prec_\Omega$—proposed by Angulo,[25] has been used:

$$c_1 \prec_\Omega c_2 = \begin{cases} d_{\mathrm{RGB}}(c_1, c_0) > d_{\mathrm{RGB}}(c_2, c_0) & \text{or} \\ d_{\mathrm{RGB}}(c_1, c_0) = d_{\mathrm{RGB}}(c_2, c_0) & \text{and} \\ \begin{cases} c_1^R < c_2^R & \text{or} \\ c_1^R = c_2^R \quad \text{and} \quad c_1^G \quad \text{or} \\ c_1^R = c_2^R \quad \text{and} \quad c_1^G = c_2^G \quad \text{and} \quad c_1^B < c_2^B \end{cases} \end{cases}, \tag{4}$$

where $d_{\mathrm{RGB}}(c_1, c_2)$ represents the distance between two points $c_1 = (c_1^R, c_1^G, c_1^B)$ and $c_2 = (c_2^R, c_2^G, c_2^B)$ in the color space RGB [see Eq. (5)] and c_0 stands for the "reference color," which in this work has been set to $c_0 = (255,255,255)$. Regarding the definition in Eq. (4), the reference color is an "upper bound" for the colors and, in the RGB color space, the intuitive "biggest color" is the white, i.e., (255, 255, 255). This is the reason why that choice for c_0 has been made. It is easy to prove that $\prec_\Omega$ is a total order relationship. This order can be used with any color space. More details about color ordering can be found in Ref. 22:

$$d_{\mathrm{RGB}}(c_1, c_2) = \sqrt{(c_1^R - c_2^R)^2 + (c_1^G - c_2^G)^2 + (c_1^B - c_2^B)^2}. \tag{5}$$

Let x be a point of the spatial support $D \subseteq \mathbb{R}^2$, the resulting classical color erosion and dilation of an image $\mathbf{f}: D \to \mathbb{R}^3$ at point x by means of a disk B_r of radius r as the structuring element (SE) is given, respectively, by

$$E_r(f)(x) = \inf_{\Omega}\{f(w): w \in B_r(x)\}, \tag{6}$$

$$D_r(f)(x) = \sup_{\Omega}\{f(w): w \in \check{B}_r(x)\}, \tag{7}$$

where $\sup_\Omega$ and $\inf_\Omega$ stand for the supremum and infimum according to the total order relationship $\prec_\Omega$. It is possible to define more advanced operators by combining dilations and erosions, such as openings, closings, alternate filters, toggle contrast, top hat, etc.

2.3 *Color Adaptive Neighborhoods and Mathematical Morphology*

The idea behind adaptive MM is to replace the classical spatially invariant (i.e., with fixed shape and size) SE by spatially variant (i.e., adaptive) SEs. In this way, the color adaptive neighborhoods (CANs)—an extension to color of the GANs,[20,26] defined in Ref. 22, can be used as adaptive SEs for color morphological operators. The color adaptive neighborhood (CAN) of a point x, denoted $V_m^f(x)$, is defined as a spatial region included in D and built upon the color image f in relation with a "homogeneity tolerance value" $m \in \mathbb{R}^+$. More precisely, $V_m^f(x)$ must fulfill the same conditions as the GANs (Sec. 2.1), i.e., (1) its points must have a color value close to the one of x and (2) the set has to be path connected, considering the usual Euclidean topology of $D \subseteq \mathbb{R}^2$.

Therefore, CANs are formally defined as

$$V_m^f(x) = C_{\{y \in D; d_{\mathrm{RGB}}(f(y), f(x)) \leq m\}}(x), \tag{8}$$

where $C_X(x)$ denotes the path-connected component of X, which contains $x \in D$, and $d_{\mathrm{RGB}}[f(y), f(x)]$ stands for the distance between the color points $f(y)$ and $f(x)$ in the color space RGB.

However, if they were used directly as adaptive structuring elements (ASEs), the symmetry property, i.e., $x \in V_m^f(y) \Leftrightarrow y \in V_m^f(x)$ may not be satisfied. Therefore, the so-called strong CANs are used as ASEs:

$$N_m^f(x) = \bigcup_{z \in D}\{V_m^f(z) | x \in V_m^f(z)\}. \tag{9}$$

Thus, the elementary adaptive morphological operators of erosion and dilation are defined, respectively, as

$$E_m(f)(x) = \inf_{\Omega}\{f(w): w \in N_m^f(x)\}, \tag{10}$$

$$D_m(f)(x) = \sup_{\Omega}\{f(w): w \in N_m^f(x)\}. \tag{11}$$

2.4 *General Adaptive Neighborhood-Based Minkowski Functionals*

Integral geometry provides a suitable family of geometrical and topological descriptors of two-dimensional (2-D) and three-dimensional (3-D) spatial patterns, known as Minkowski functionals.[27] In 2-D, there are three Minkowski functionals: area, perimeter, and Euler number, denoted as A, P, and χ, respectively.

These functionals are defined on the class of nonempty compact convex sets in $\mathbb{R}^2$. They have been extended to the convex ring,[28] i.e., the set of all finite unions of convex bodies, which may be considered as a realistic Euclidean model for digital images. In this paper, the densities of these functionals are used (i.e., the functionals are normalized by the area of the spatial support D). The densities of the area, perimeter, and Euler number are denoted as A_A, P_A, and χ_A, respectively.

The GAN-based Minkowski maps[29] are defined by assigning to each point $x \in D$ the Minkowski density functional of its GAN $V_m^h(x)$. More explicitly, the GAN-based Minkowski map of a gray-level image, denoted by μ_m^h, is defined by

$$\mu_m^h(x) = \mu[V_m^h(x)], \tag{12}$$

where μ denotes a Minkowski density functional (i.e., $\mu \equiv A_A$, $\mu \equiv P_A$, or $\mu \equiv \chi_A$).

Figure 3 shows an example of GAN-based Minkowski map of an image using the area as the functional. The GANs are homogeneous with respect to the luminance of the blue color component using the tolerance $m = 20$. Therefore, the value at each point x of the Minkowski map is the area of the GAN $V_{20}^h(x)$.

2.5 *Local Binary Patterns*

LBPs were introduced by Ojala et al.[17] This original version worked in a 3×3 pixel block of an image and was later generalized[18] to remove any limitations on size of the neighbor or the number of sampling points. LBP is a gray level texture descriptor that extracts the local spatial structure of an image. Given a pixel, a pattern code is computed by comparing it with the value of its neighbors, as stated in Eq. (13).

$$\mathrm{LBP}_{P,R}(x_c, y_c) = \sum_{p=0}^{P-1} s(g_p - g_c) 2^p, \tag{13}$$

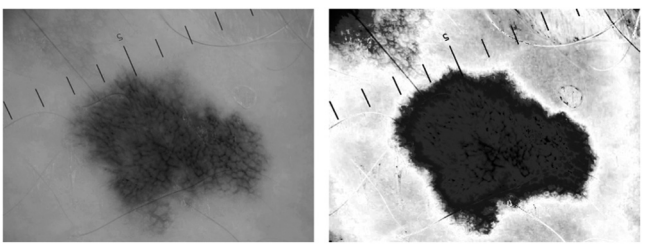

(a) (b)

Fig. 3 The GAN-based area map (b) of the green component (a) of a dermoscopic image computed with the luminance criterion and the homogeneity tolerance value $m = 20$.

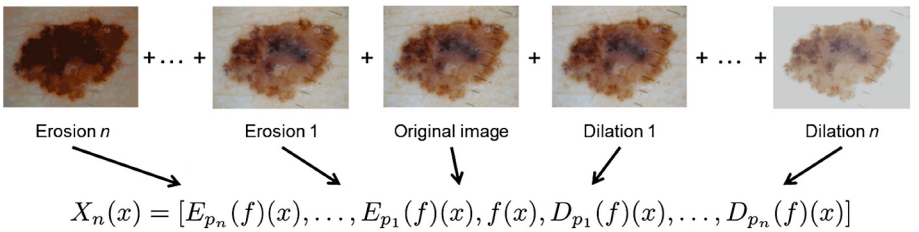

Fig. 4 Illustration of the concatenation of color components to form the pixel descriptor using color adaptive MM.

where g_c is the value of the central pixel (x_c, y_c), g_p is the value of its p'th neighbor, P is the number of neighbors, and R is the radius of the neighborhood. The function $s(z)$ is defined as

$$s(z) = \begin{cases} 1, & z \geq 0 \\ 0, & z < 0 \end{cases} 3 \tag{14}$$

Finally, the whole image is described by means of a histogram of the LBP values of all pixels.

3 Proposed Descriptors

In this work we propose two texture descriptors of the color images: the first one is based on color MM and SOMs, and the other one is based on LBPs computed on the GAN-Minkowski maps of the R, G, and B components of the images.

3.1 *Color Adaptive Neighborhood MM-Based Descriptor*

The first color adaptive neighborhood MM (CANMM)-based descriptor is computed in two steps. First of all, the images are described locally, based on the chromatic information of each point in several successive dilations and erosions. Afterwards these local descriptors are used to describe the image globally by means of an SOM.[23]

3.1.1 *Pixel-level description*

The descriptors of each pixel consist on a concatenation of (1) its color components in the original image and (2) the color components of the same point in multiscale dilations and erosions (i.e., using SEs of different sizes p_i). For classical (resp. adaptive) MM, p_i denotes the radius (resp. homogeneity tolerance) of the SE (resp. ASE).

Therefore, the general expression (i.e., for either classical or adaptive MM) of the descriptor of each pixel $x \in D$ is

$$X_n(x) = [E_{p_n}(f)(x), \ldots, E_{p_1}(f)(x), f(x), D_{p_1}(f)(x), \ldots, D_{p_n}(f)(x)], \tag{15}$$

where n stands for the number of erosions and dilations which are carried out, $f(x)$ represents the values of the color components of the image f at x, and $E_{p_i}(f)(x)$ (resp. $D_{p_i}(f)(x)$) represents the values of the color components at x of the erosions (resp. dilations) of f with a SE with size or tolerance p_i. Figure 4 shows an illustration of such a concatenation.

3.1.2 *Global image descriptor*

Once the pixels of an image are described, a "global" descriptor of that image is built. This is done by means of a Kohonen SOM.[23] This map has been generated by means of 20 images selected by experts (i.e., 10 representative images of each class), from which the lesions were roughly segmented manually. Thereafter, the map was generated in a training step using the pixels of the lesions and 5% of the other pixels (randomly selected). Note that this segmentation is only used for these 20 "training" images.

Afterward, the pixels of the image are projected onto the neurons of the map in order to cluster them. Finally, the final image descriptor is the histogram of the hits of the neurons, i.e., the number of pixels that have been projected on each neuron of the map.

A diagram showing the description process is shown in Fig. 5.

3.2 *General Adaptive Neighborhood-Minkowski Local Binary Pattern Descriptor*

The proposed texture descriptor based on LBP is built in two steps.

First of all, the GAN-based Minkowski map μ_m^h of the different color components R, G, and B of the original color image is computed. Thereafter, the $\text{LBP}_{P,R}$ operator Eq. (7) of each of these maps is computed, and the three histograms are concatenated. A graphic description of this process is shown in Fig. 6.

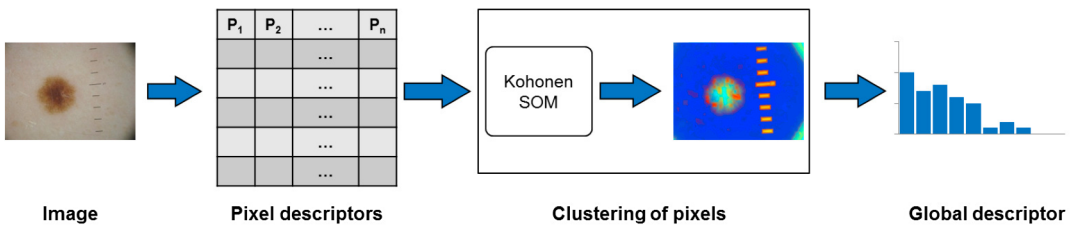

Fig. 5 Flow diagram of the image description process.

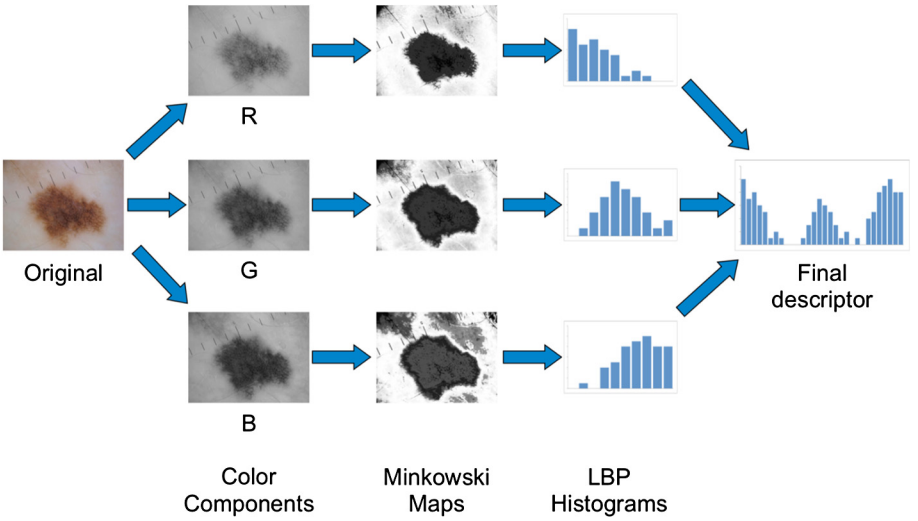

Fig. 6 Image description process.

4 Experiments and Results

4.1 *Experiments*

4.1.1 *Image database*

The image dataset that has been used in this experiment was composed of 1097 dermoscopic images of pigmented skin lesions with 88 of them being histopathologically confirmed melanomas. Thus, two classes were considered in this experiment: on one hand, confirmed melanomas, and on the other hand, the remaining benign lesions.

All images were acquired by several dermatologists equipped with a digital camera (SONY W120) combined with a Heine Delta 20 dermoscope. After the acquisition was carried out, the images were normalized so that they have the same pixel size.

4.1.2 *Image descriptors*

Three different experiments have been done in this work, using either the CANMM-based descriptor (Sec. 3.1), the GAN-Minkowski LBP descriptor (Sec. 3.2), or a combination of both.

First of all, concerning the descriptor based on color MM, the local pixel descriptor described in Sec. 3.1.1 has been computed using (1) the adaptive CAN-based erosions and dilations and (2) classical (i.e., nonadaptive) erosions and dilations, for the sake of comparison. In this case, a square-shaped SE has been used, with width sizes varying between 5 and 50 in steps of 5. In the case of the adaptive CAN-based erosions and dilations, the values for the tolerance m varied from 5 to 50 in steps of 5. Therefore, in both cases, 10 different erosions and dilations were carried out so each pixel was described by means of 63 features (i.e., the RGB components of the pixel in the original image and its components after the erosions and dilations). Afterward, a Kohonen map of size 20×20 pixels was used, as explained in Sec. 3.1.2. Therefore, each image has been described by means of a feature vector of 400 elements.

Considering the descriptor based on the LBP of the CAN-based Minkowski maps, as was explained in Sec. 3.2, each of the color components R, G, and B of the images of skin lesions has been considered as a gray-level image. First of all, the GAN-based Minkowski map "area" with a tolerance of 20 was computed from each of them (i.e., A_{20}^{R}, A_{20}^{G}, and A_{20}^{B}). The other two Minkowski functionals P and χ, as well as different tolerances m were assessed, but they yielded worse results. After that, the $\mathrm{LBP}_{P,R}$ was computed from each of these three area maps. The number of samples P was fixed to 8, but different possible values for the radius R were assessed (specifically, they varied from 1 to 6). Thus, the LBP histogram of each component has a length of 256. The final descriptor is a concatenation of the three LBP histograms (i.e., the final descriptor has 768 features). For the sake of comparison, another descriptor, where the $\mathrm{LBP}_{P,R}$ operator was computed directly on the intensities of the color components R, G, and B, has been assessed.

Finally, a concatenation of these two proposed descriptors has been considered, both the adaptive (i.e., the CANMM-based concatenated with the GAN-Minkowski LBP descriptors) and the "classic" versions (i.e., the first descriptor computed with nonadaptive MM concatenated with the $\mathrm{LBP}_{P,R}$ of the intensities of the color components R, G, and B). This combined descriptor has 1168 features/image.

4.1.3 *Classification*

Images were subsequently classified by means of a feed-forward artificial neural network working on their feature vectors. The data were normalized before classification, so that they had mean 0 and standard deviation 1. In this experiment, a network with one hidden layer and a logistic sigmoid activation function for the hidden and output layers have been employed. The learning of the network was carried out with the momentum and adaptive learning rate algorithm. Different combinations of training cycles and neurons in the hidden layer have been used in order to assess the impact of this configuration on the results. The classification was carried out using stratified 10-fold cross validation, and the process was repeated 10 times in order to avoid possible random effects (e.g., due to the random initialization of the network) and overfitting. The presented results are an average of these 10 runs.

4.2 *Results*

It is necessary to remark that no preprocessing of the data was done in order to prevent the bias of the classifier toward the majority class. However, as the dataset is highly imbalanced toward the benign lesion class, the receiver operating characteristics (ROC) curve is more suitable to illustrate the performance of a classifier than the accuracy of the classification.[30] It is also widely used in visualizing and analyzing the behavior of diagnostic systems. It summarizes the classifier performance over a range of tradeoffs (i.e., decision thresholds) between benefits (i.e., true positives or sensitivity) and costs (i.e., false positives or 1-specificity).[31] More details about ROC curves can be found in Ref. 30.

A measure that summarizes how good this curve is, is the area under the ROC curve (AUC). In the case of the descriptors based on MM, the neural network configurations (i.e., neurons in the hidden layer and training cycles) that achieved the "best" results were 300 cycles and 7 neurons, and 400 cycles and 9 neurons for the classical and adaptive approaches with AUCs of 0.859 and 0.854, respectively. In addition, Tables 1 and 2 show the AUC in the "best" classification scenario (i.e., the best configuration of the neural network) achieved by the descriptors based on the LBP computed directly on the intensities of the color components and computed on the GAN-area maps, respectively, depending on the different assessed values of R. The highest AUC is shown in bold.

Figure 7 depicts the ROC curves of these classifiers along with a mean ROC curve estimated in Ref. 16 from the predictions carried out by nine dermatologists with this same image dataset. The AUC of this curve is 0.792.

Overall, both classifiers based on MM (classical and adaptive) are comparable. The classifier generated by means of the descriptor based on classic MM slightly outperforms the CAN-based one, obtaining AUCs of 0.859 and 0.854, respectively. The descriptors based on the LBP outperform them, with AUCs of 0.8948 and 0.9115 for the classical and GAN-area-based ones, respectively. According to the latter, the sensitivity and specificity of the classifier were 98.41% and 38.64%, respectively. Any of the descriptors proposed in this paper generated, without any segmentation step, classifiers which outperformed the actual predictions of the dermatologists. In particular, the classifiers were found to be particularly efficient in the distal part of the ROC curves, where the detection of the remaining melanoma is difficult.

Other works that deal with the problem of melanoma detection in the literature report similar sensitivities and higher specificities than the ones achieved in this work. For example, Tenenhaus et al.[8] reported a sensitivity of 95% and a specificity of 60%, although the overall AUC that their classifier achieved was 0.84. Amelard et al.[10] obtained a sensitivity and a specificity of 92.52% and 73.45%, respectively, and Rastgoo et al.[11] obtained 98% and 70% of sensitivity and specificity, respectively. However, let us remember that in this case, previous segmentation of the lesions is not carried out and, what is more important, the dataset is highly imbalanced—only 8% of the images are melanoma—while in the case of these works, the datasets are either balanced or the proportion of melanoma is 30%. Wazaefi et al.[16] did use the same dataset that was used in this paper, and their classifier achieved an AUC of 0.885. However, Korotkov and Garcia[6] pointed out that the absence of benchmark datasets

Table 1 Area under the ROC curve (AUC) of the best combination cycles-neurons in the artificial neural network (ANN) for the descriptors based on the "classical" local binary pattern (LBP).

R	No. of neurons	No. of cycles	AUC
1	10	300	0.8726
2	7	300	**0.8948**
3	7	400	0.8934
4	5	500	0.8946
5	7	400	0.8895
6	10	400	0.8898

The highest AUC is shown in bold.

Table 2 AUC of the best combination cycles-neurons in the ANN for the descriptors based on the general adaptive neighborhood-area-based LBP.

R	No. of neurons	No. of cycles	AUC
1	10	500	0.8547
2	10	500	0.8780
3	10	500	0.8934
4	7	300	0.8976
5	10	500	0.9052
6	10	500	**0.9115**

The highest AUC is shown in bold.

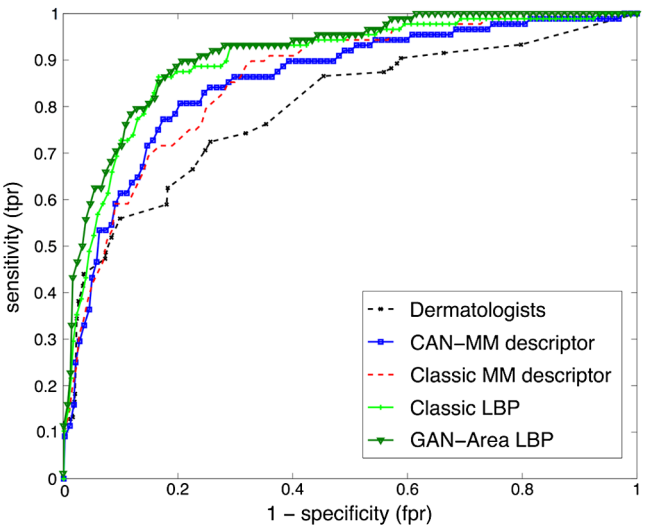

Fig. 7 Receiver operating characteristics (ROC) curve of the classifiers generated by means of the classic MM, color adaptive neighborhood (CAN)-based MM, "classical" and GAN-area-based local binary pattern (LBP), together with the mean ROC curve observed for the dermatologists.

Table 3 AUC of the best combination cycles-neurons in the ANN for the adaptive concatenated descriptors.

R	No. of neurons	No. of cycles	AUC
1	7	300	0.8604
2	5	300	0.8660
3	5	300	0.8699
4	5	300	0.8729
5	5	400	**0.8799**
6	5	300	0.8771

The highest AUC is shown in bold.

for standardized algorithm evaluation makes it difficult to compare different works.

4.2.1 *Results with combined descriptors*

The concatenation of both the "adaptive" and "classical" (i.e., nonadaptive) descriptors was classified following the same experimental configuration as the proposed ones.

As done in previous section, Tables 3 and 4 show the AUC in the "best" classification scenario achieved by the concatenated descriptors in their adaptive and nonadaptive versions, respectively, depending on the different assessed values of R. The highest AUC is shown in bold.

It is remarkable than the nonadaptive version of these concatenated descriptors performs better than the adaptive one. A possible explanation is that, although the adaptive version of LBP shows a better performance than the "classic" one (AUCs 0.9115 against 0.8948), the nonadaptive MM-based descriptors slightly outperformed the adaptive one (0.859 and 0.854, respectively). Consequently, it seems that the MM-based descriptor has more weight for the classifier. Anyway, both versions of the concatenated descriptors obtained better results than the dermatologists, the MM based descriptors (both the adaptive and nonadaptive), and the "classical" LBP-based descriptors. Still they do not outperform the adaptive LBP-based descriptors.

Table 4 AUC of the best combination cycles-neurons in the ANN for the "classical" concatenated descriptors.

R	No. of neurons	No. of cycles	AUC
1	5	300	0.8790
2	7	300	0.8928
3	10	300	0.8946
4	5	300	**0.8968**
5	5	300	0.8877
6	10	300	0.8865

The highest AUC is shown in bold.

Processing high dimensional data is computationally expensive and due to possible correlations in the data (e.g., the colors of some dilations and erosions might be similar), it is also inefficient. Therefore, a dimensionality reduction using principal component analysis[32] has been carried out, with a number of principal components up to 20 (more than 10 were enough in all cases to explain more than 99% of the variance of the dataset). However, the results using these "reduced" data were worse than the "nonreduced" version.

5 Conclusions and Future Perspectives

In this work, two texture descriptors have been introduced and applied to the description and classification of images of naevi as benign lesions or melanoma. The first one is built from the local color data of each pixel, obtained from MM operations. It is afterward used to describe the image globally by means of Kohonen SOMs. Two approaches of this descriptor have been assessed: (1) the local data has been obtained using the classic (i.e., nonadaptive) color MM operations and (2) getting this local data by means of adaptive color MM based on the CAN framework. The second descriptor is computed from LBP and local geometrical features (the Minkowski functionals) computed from the GANs of each color component of the image. Its performance has been compared with the classical LBP computed from the intensities of each color component.

The best performance has been obtained by the GAN-Minkowski based LBPs, using the area and a tolerance for the GANs equals to 20. The number of samples of the LBPs was fixed to 8 and the radius R varied, with the best results achieved for $R = 6$. This GAN approach achieved an AUC of 0.912, whereas the classical approach achieved an AUC of 0.895. The descriptors based on MM achieved similar performances, getting AUCs of 0.859 and 0.854 in the case of the nonadaptive and adaptive approaches, respectively. Any of these descriptors outperformed the dermatologists' predictions on the same image dataset, which obtained an average ROC curve with an AUC of 0.792.[16]

For future work, other GAN-based geometrical and/or morphometrical features[33] applied to this problem will be investigated.

Acknowledgments

This work has been supported by the project with reference ANR-12-EMMA-0046 from the French National Research Agency.

References

1. F. Nachbar et al., "The ABCD rule of dermatoscopy: High prospective value in the diagnosis of doubtful melanocytic skin lesions," *J. Am. Acad. Dermatol.* **30**, 551–559 (1994).
2. R. H. Johr, "Dermoscopy: alternative melanocytic algorithms—the ABCD rule of dermatoscopy, menzies scoring method, and 7-point checklist," *Clin. Dermatol.* **20**, 240–247 (2002).
3. R. B. Aldridge et al., "Novice identification of melanoma: Not quite as straightforward as the abcds," *Acta Dermato Venereol.* **91**, 125–130 (2011).
4. K. McLaughlin, R. Rikers, and H. Schmidt, "Is analytic information processing a feature of expertise in medicine?," *Adv. Health Sci. Educ.* **13**(1), 123–128 (2008).
5. G. Norman, "Building on experience the development of clinical reasoning," *N. Engl. J. Med.* **355**(21), 2251–2252 (2006).
6. K. Korotkov and R. Garcia, "Computerized analysis of pigmented skin lesions: a review," *Artif. Intell. Med.* **56**(2), 69–90 (2012).
7. T. Tanaka et al., "A study on the image diagnosis of melanoma," in *26th Annual Int. Conf. of the IEEE Engineering in Medicine and Biology Society*, Vol. 1, pp. 1597–1600 (2004).

8. A. Tenenhaus et al., "Detection of melanoma from dermoscopic images of naevi acquired under uncontrolled conditions," *Skin Res. Technol.* **16**(1), 85–97 (2010).
9. A. G. Isasi, B. G. Zapirain, and A. M. Zorrilla, "Melanomas non-invasive diagnosis application based on the ABCD rule and pattern recognition image processing algorithms," *Comp. Biol. Med.* **41**(9), 742–755 (2011).
10. R. Amelard et al., "High-level intuitive features (HLIFs) for intuitive skin lesion description," *IEEE Trans. Biomed. Eng.* **62**, 820–831 (2015).
11. M. Rastgoo et al., "Automatic differentiation of melanoma from dysplastic nevi," *Comp. Med. Imaging Graph.* **43**(0), 44–52 (2015).
12. M. Zortea et al., "Automatic segmentation of dermoscopic images by iterative classification," *Int. J. Biomed. Imaging* **2011**, 972648 (2011).
13. J. Glaister, A. Wong, and D. Clausi, "Segmentation of skin lesions from digital images using joint statistical texture distinctiveness," *IEEE Trans. Biomed. Eng.* **61**, 1220–1230 (2014).
14. M. Celebi et al., "Lesion border detection in dermoscopy images," *Comp. Med. Imaging Graph.* **33**(2), 148–153 (2009).
15. B. Erkol et al., "Automatic lesion boundary detection in dermoscopy images using gradient vector flow snakes," *Skin Res. Technol.* **11**(1), 17–26 (2005).
16. Y. Wazaefi, S. Paris, and B. Fertil, "Contribution of a classifier of skin lesions to the dermatologist's decision," in *3rd Int. Conf. on Image Processing Theory, Tools and Applications*, pp. 207–211 (2012).
17. T. Ojala, M. Pietikäinen, and D. Harwood, "A comparative study of texture measures with classification based on featured distributions," *Pattern Recognit.* **29**(1), 51–59 (1996).
18. T. Ojala, M. Pietikäainen, and T. Maenpaa, "Multiresolution gray-scale and rotation invariant texture classification with local binary patterns," *IEEE Trans. Pattern Anal. Mach. Intell.* **24**, 971–987 (2002).
19. M. Pietikäinen et al., *Computer Vision Using Local Binary Patterns*, Springer, London (2011).
20. J. Debayle and J.-C. Pinoli, "General adaptive neighborhood image processing: part I: introduction and theoretical aspects," *J. Math. Imaging Vision* **25**, 245–266 (2006).
21. J.-C. Pinoli and J. Debayle, "General adaptive neighborhood mathematical morphology," in *16th IEEE Int. Conf. on Image Processing*, pp. 2249–2252 (2009).
22. V. González-Castro, J. Debayle, and J.-C. Pinoli, "Color adaptive neighborhood mathematical morphology and its application to pixel-level classification," *Pattern Recognit. Lett.* **47**, 50–62 (2014).
23. T. Kohonen, *Self-Organizing Maps*, Springer Series in Information Sciences, Vol. **30**, Springer-Verlag, Berlin, Heidelberg (1997).
24. J. Serra, *Image Analysis and Mathematical Morphology*, Academic Press, New York (1982).
25. J. Angulo, "Morphological colour operators in totally ordered lattices based on distances: application to image filtering, enhancement and analysis," *Comp. Vision Image Understand.* **107**(1–2), 56–73 (2007).
26. J. Debayle and J.-C. Pinoli, "General adaptive neighborhood image processing: part II: practical application examples," *J. Math. Imaging Vision* **25**(2), 267–284 (2006).
27. K. Michielsen and H. De Raedt, "Integral-geometry morphological image analysis," *Phys. Rep.* **347**(6), 461–538 (2001).
28. K. Mecke and D. Stoyan, *Statistical Physics and Spatial Statistics*, Springer-Verlag, Berlin, Heidelberg (2000).
29. S. Rivollier, J. Debayle, and J.-C. Pinoli, "Integral geometry and general adaptive neighborhood for multiscale image analysis," *Int. J. Signal Image Process.* **1**(3), 141–150 (2010).
30. T. Fawcett, "An introduction to ROC analysis," *Pattern Recognit. Lett.* **27**, 861–874 (2006).
31. N. Chawla, "Data mining for imbalanced datasets: an overview," in *Data Mining and Knowledge Discovery Handbook*, O. Maimon and L. Rokach, Eds., pp. 853–867, Springer, United States (2005).
32. J. Jackson, *A User's Guide to Principal Components*, Wiley Series in Probability and Mathematical Statistics, Wiley, Hoboken, New Jersey (1991).
33. S. Rivollier, J. Debayle, and J.-C. Pinoli, "Adaptive shape diagrams for multiscale morphometrical image analysis," *J. Math. Imaging Vision* **49**(1), 51–68 (2014).

Víctor González-Castro received his PhD in 2011 from the University of León, working in image processing applied to semen quality control. He worked as a postdoctoral research assistant in the École des Mines de Saint-Étienne (France) in adaptive mathematical morphology applied to classification of skin lesions. He is currently working as a lecturer in medical image analysis in the Centre for Clinical Brain Sciences of the University of Edinburgh. His research interests include image processing and pattern recognition applied to biomedical problems.

Johan Debayle received his PhD degree in the field of image processing in 2005 from MINES Saint-Etienne, France. In 2006, he joined INRIA, Sophia-Antipolis, France, as a postdoctoral fellow. Since 2007, he is an associate professor at MINES Saint-Etienne. In 2012, he received the HDR from UJM Saint-Etienne, France. In 2015, he was nominated senior member of the IEEE. His research interests include adaptive image processing, pattern analysis and stochastic geometry.

Yanal Wazaefi is currently working as a data scientist at Kelkoo. Before joining Kelkoo, he was a research engineer at LSIS, where he worked on a computer-aided diagnosis system of melanoma using machine learning methods applied on dermoscopic images of lesions. Before that, he was a PhD candidate at Aix-Marseille University, where he worked as a research engineer at VISOON-Lyon in collaboration with the Images and Models team at LSIS-Marseille. During his PhD, he taught some courses at the university as a teaching assistant.

Mehdi Rahim received the MSc degree in computer science in 2008 and his PhD in 2012 from the Aix-Marseille University (France). His thesis was on shape analysis applied to the characterization of pelvic diseases. Since 2014, he has been a postdoctoral fellow at the French Atomic Energy Commission (CEA) in the field of the neuroimaging and machine learning. His research interests are image processing and machine learning for medical image analysis.

Caroline Gaudy-Marqueste is an associate professor in the Dermatology and Skin Cancer Department headed by Pr Jean-Jacques Grob in Marseille since 2009. She obtained an MD in biology in 2004 and a PhD in human genetics in 2009 and is a member of the UMRS911 CRO2 Research Unit since 2010. She is specialized in melanoma management and prevention and interested in the study of melanoma epidemiology and the molecular characterization of aggressive forms of the disease.

Jean-Jacques Grob is head of the Dermatology and Skin Cancer Department in Marseille France, at the Timone APHM University Hospital and Aix-Marseille University. His main research interests include skin cancers and melanoma, namely epidemiology, prevention, early diagnosis, and evaluation of new treatments of advanced disease. He is an author of more than 240 articles registered in the MEDLINE database.

Bernard Fertil received the PhD degree in physics from Paris XI University, Paris, France, in 1975 and in living sciences from Paris VI University, Paris, France, in 1984. Currently, he is a research director at the CNRS institute, heading Group 4 of INSERM unit 678 in Paris, France. He is the author or coauthor of more than 120 scientific papers. His research interests include data mining, image analysis, and modeling, with specific applications to medical decision making, bioinformatics, and radiobiology.